

# Long-Range Correlations in Self-Gravitating $N$ -Body Systems

Daniel Huber and Daniel Pfenniger

Geneva Observatory, CH-1290 Sauverny, Switzerland

Received July 2001 / Accepted January 2002

**Abstract.** Observed self-gravitating systems reveal often fragmented non-equilibrium structures that feature characteristic long-range correlations. However, models accounting for non-linear structure growth are not always consistent with observations and a better understanding of self-gravitating  $N$ -body systems appears necessary. Because unstable gravitating systems are sensitive to non-gravitational perturbations we study the effect of different dissipative factors as well as different small and large scale boundary conditions on idealized  $N$ -body systems. We find, in the interval of negative specific heat, equilibrium properties differing from theoretical predictions made for gravo-thermal systems, substantiating the importance of microscopic physics and the lack of consistent theoretical tools to describe self-gravitating gas. Also, in the interval of negative specific heat, yet outside of equilibrium, unforced systems fragment and establish transient long-range correlations. The strength of these correlations depends on the degree of granularity, suggesting to make the resolution of mass and force coherent. Finally, persistent correlations appear in model systems subject to an energy flow.

**Key words.** Gravitation - Methods:  $N$ -body simulations - Galaxies: ISM - ISM: structure

## 1. Introduction

Most astrophysical structures result of gravitational instabilities, from large scale cosmological structures down to planets. Yet, among the least understood topics in astrophysics we find galaxy formation and star formation, which both involve fragmentation and the nonlinear growth of structures occurring during the non-linear phases of gravitational instability.

Perhaps, one of the fundamental reason why fragmentation and structure formation via gravitational instability appears so difficult is that we lack of consistent theoretical tools allowing to combine gravity with gas physics. Indeed, too often ignored is that classical thermodynamics does not hold for gravitating systems, because these are non-extensive in the thermodynamical sense (Landsberg 1972,1984; Tsallis 1999; Plastino & Plastino 1999). Actually, many other natural systems do not respect the requisites of thermodynamics. Such systems often feature interesting phenomena such as growing long range correlations or phase transitions. Among the symptoms of a fundamental deep problem in gravitating systems is the appearance of negative specific heat (Lynden-Bell & Lynden-Bell 1977; Lynden-Bell 1998), which was seen for a long time as a paradox in statistical mechanics, since negative specific heat was thought to be impossible.

Presently, the only available approach to follow the nonlinear phases of gravitational instabilities is to carry out numerical simulations. Among all the existing methods,  $N$ -body techniques are thought to be the most effective to simulate self-gravitating systems as well the continuous case as the granular phases.

Yet, despite the considerable success of these methods in reproducing many observed features, many fundamental problems remain. As mentioned above, the fragmentation and structure formation is not clearly understood. Related to this, CDM simulations conflict with observations at galactic scales (Moore 1999, James et al. 2001, Bolatto et al. 2002), and no theory of the ISM is presently able to *predict* the conditions of star formation. Most of the time the star formation process relies on recipes with little physical constraint.

In situations where  $N$ -body simulations have success (e.g. hot stellar systems) gravitational dynamics is sufficient to account for their main global properties, additional microscopic physics can be neglected. But when gravitational instability via fragmentation involves small scale physics, the outcome may be strongly dependent on the properties of the small scale physics. In other words, in situations where the growth on singularities triggered by gravity is allowed, the chaotic nature of gravitating systems make them sensitive to the perturbations induced by non-gravitational physics.

Therefore it is important to understand the properties of  $N$ -body systems subjected to various perturbations.

For these purposes, a numerical study of perturbed, self-gravitating  $N$ -body systems is carried out.

Among the relevant perturbations we expect that boundary conditions at small and large scales, as well as dissipative factors can play a key role. In order to characterize the individual effects of perturbations, in the tradition of analytical models, one is advised to deliberately use simplified models.

A study of dissipative systems is important because such systems may develop long-range correlations. In the typical ISM, radiative cooling is very effective and induces a temporary energy-flow leading the system far from equilibrium (Dyson & Williams 1997). From laboratory experiments it is well known that systems outside of equilibrium may spontaneously develop spatio-temporal structures (Glandsdorff & Prigogine 1971; Nicolis & Prigogine 1977; Prigogine 1980; Melo 1994).

A permanent energy-flow is induced when energy loss due to dissipation is replenished, that is, when the system is continuously driven, e.g., by time-dependent boundary conditions. Such systems may develop persistent long-range correlations. Astrophysical examples for this are, the growth of structures in cosmological simulations, or the long term persistence of filamentary structures in shearing flows (Toomre & Kalnajs 1991; Huber & Pfenniger 2001a; Wisdom & Tremaine 1988; Salo 1995; Pfenniger 1998). Among other things, the effect of time-dependent potential perturbations on dissipative self-gravitating spheres is studied in this paper.

In the next Section we briefly review some theoretical results of the thermodynamics of self-gravitating isothermal spheres. The model is presented in Sect. 3 and the applied methods to carry out the structure analysis for the simulated systems are explained in Sect. 4. The results are presented in Sect. 5-7. In Sect. 5 quasi-equilibrium states of  $N$ -body models are compared with analytical predictions. Sect. 6 is dedicated to a study of long-range correlations appearing in the interval of negative specific heat during the collapsing transition of gravitating systems. Finally, in Sect. 7 the evolution of systems subjected to an energy-flow is discussed.

## 2. Gravo-thermal Statistics

By confining a gravitational system within a sphere, we can compare our numerical work with previous analytical studies using the tools of statistical mechanics and point out some discrepancies. Although the theory, sometimes referred to as gravo-thermal statistics, is not fully consistent, since the applied Gibbs-Boltzmann entropy is derived under the assumption of extensivity (Taruya & Sakagami 2001), it yields some important and instructive results.

Before we present the model and the results let us here briefly review some theoretical findings (see Padmanabhan 1990 for an extended discussion on the topic).

Antonov (1962) and Lynden-Bell & Wood (1968) studied theoretically the thermodynamics of self-gravitating

isothermal spheres and found anomalous behavior when compared with classical thermodynamics of extensive systems. An example of such an anomalous behavior is the so called gravo-thermal catastrophe that occurs when an isothermal gas of energy  $E(< 0)$  and mass  $M$  is released within a spherical box of radius greater than Antonov's radius,  $r_A = 0.335GM^2/(-E)$ . The analytical model predicts that for such systems there is no equilibrium to go and nothing can stop the collapse of the central parts.

Antonov's and Lynden-Bell & Wood's investigations based on point-like particles. Since then several studies were carried out with modified (i.e., non point-like) particle potentials. Hertel & Thirring (1971) modified the gravitational interaction potential by introducing short-distance repulsive forces due to quantum degeneracy and Aronson & Hansen (1972) investigated the behavior of self-gravitating hard-spheres. Finally, Follana & Laliena (2000) applied softened interaction potentials. They found all qualitatively the same result: Unlike the model of Lynden-Bell & Wood, there is always an equilibrium state for finite size particles. However, a phase transition, separating a high energy homogeneous phase from a low energy collapsing phase with core-halo structure occurs in an energy interval with negative microcanonical specific heat,

$$c_V = \left( \frac{\partial \varepsilon}{\partial T} \right)_V = -\beta^2 \left( \frac{\partial \varepsilon}{\partial \beta} \right)_V < 0, \quad (1)$$

where  $\varepsilon$  is the total energy and  $\beta = 1/T$  is the inverse temperature.

There are fewer theoretical works done with the grand canonical ensemble (e.g. de Vega, Sanchez & Combes 1996) where mass would be allowed to be exchanged with the environment, therefore we limit the scope of this study to the canonical ensemble, that is energy can be exchanged with the environment, but not the mass and angular momentum.

Note that an ensemble allowing to exchange also angular momentum would be very relevant for astrophysical situations, but few theoretical works have been made on this important aspect (Laliena 1999; Fliegans & Gross 2001).

## 3. Model

A spatially isolated, spherical  $N$ -body system is studied. The  $N$  particles of the system are accelerated by gravity and forces induced by boundary conditions and perturbations, respectively. In all, a particle can be accelerated by five force types: 1.) confinement 2.) energy dissipation due to velocity dependent friction 3.) external forcing 4.) long range attraction (self-gravity) and 5.) short range repulsion. The five force types are discussed in detail in Sects. 3.2-3.5.

### 3.1. Units

A steep potential well confines the particles to a sphere of radius  $R \approx 1$  (see Sect. 3.2). The total mass  $M$  and the gravitational constant  $G$  are equal one as well,  $G = M = 1$ . The dimensionless energy is the energy measured in units of  $GM^2/R$ , that is in our model  $\approx 1$ . Thus energies and other quantities with energy dimension (like the temperature) can be considered as dimensionless.

### 3.2. Confinement

In order to keep the model simple and to enable a comparison with established theoretical results of canonical isothermal spheres we apply a confinement that prevents gravitationally unbound particles from escape and keeps thus the particle number constant.

The confinement is realized through a steep potential well

$$\Phi_{\text{conf}} \propto R^{16}, \quad (2)$$

where  $R$  is the distance from the center of our spatially isolated system. The walls of the potential well are steep, so that the particles are only significantly accelerated by the confinement when they approach  $R = 1$ . However, the potential walls must not be too steep, to avoid unphysical accelerations near the wall, due to a discrete time-step.

Contrary, to non-spherical reflecting enclosures the applied potential well conserves angular momentum.

### 3.3. Energy Dissipation

The effect of different dissipation schemes is studied: Local dissipation, global dissipation and a scheme similar to dynamical friction. For convenience we call the latter hereafter “dynamical friction”.

#### 3.3.1. Local Dissipation

The local dissipation scheme represents inelastic scattering of interstellar gas constituents. That is, friction forces are added, that depend on the relative velocities and positions of the neighboring particles.

A particle is considered as a neighbor if its distance is  $r < \lambda\epsilon$ , where  $\epsilon$  is the softening length and  $\lambda$  is a free parameter. The friction force has the form:

$$F_i = \begin{cases} \Lambda \frac{m^2 r_i}{(r^2 + \epsilon^2)^{3/2}} r^{2-\eta} \left( \frac{\mathbf{V} \cdot \mathbf{r}}{r} \right)^\zeta & : r < \lambda\epsilon \text{ and } \mathbf{V} \cdot \mathbf{r} < 0 \\ 0 & : \text{otherwise,} \end{cases} \quad (3)$$

where  $V$  is the relative velocity of two neighboring particles,  $\zeta, \eta \geq 0$  are free parameters and  $i = x, y, z$ . The term  $\mathbf{V} \cdot \mathbf{r}/r = V \cos \vartheta < 0$  ensures a convergent flow and that dissipation affects only the linear momentum. As a consequence angular momentum is locally conserved.

For  $\epsilon \ll r < \lambda\epsilon$  the friction force is,

$$F_i \propto \frac{(V \cos \vartheta)^\zeta}{r^\eta} e_i, \quad (4)$$

where  $e_i$  is the  $i$ th component of the unity vector. Thus the friction force increases with the relative velocity and decreases with the distance, provided that  $\zeta, \eta > 0$ . The condition  $r < \lambda\epsilon$  ensures the local nature of the energy dissipation.

#### 3.3.2. Global Dissipation

The global dissipation depends not on the relative velocity  $V$ , but on the absolute particle velocity  $v$ . The global friction force is,

$$F_i = -\alpha v_i, \quad (5)$$

where  $\alpha$  is a free parameter. The same friction force was already used in the shearing box experiments of Toomre & Kalnajs (1991) and Huber & Pfenniger (2001a, 2001b).

#### 3.3.3. Dynamical Friction

Setting the velocity-dispersion  $\sigma = 1$ , which is the dispersion of a virialized self-gravitating system with  $M = R = 1$ , Chandrasekhar dynamical friction formula can be parameterized in good approximation by,

$$F_i = \Gamma \frac{v_i}{(4 + v^3)}, \quad (6)$$

where  $\Gamma$  is a free parameter (Chandrasekhar 1943; Binney & Tremaine 1994). In contrast to global dissipation this scheme has the feature that  $F_i$  does not increase asymptotically with  $v$ . There is a maximum at  $v \approx 1.3$ . Thus high speed particles in collapsed regions dissipate no longer energy and gravitational runaway is impeded.

### 3.4. Forcing Scheme

If the dissipated energy is replenished by a forcing scheme the system can be subjected to a continuous energy-flow. Here the energy injection is due to time-dependent boundary conditions, that is, due to a perturbation potential. This perturbation should on the one hand be non-periodic and quasi-stochastic, on the other hand it should provide approximately a regular large-scale energy injection in time average. A simple perturbation potential, meeting these conditions, has the linear form,

$$\Phi_{\text{pert}}(x, y, z, t) = \gamma [B_x(t)x + B_y(t)y + B_z(t)z], \quad (7)$$

where  $x, y$  and  $z$  are Cartesian coordinates,  $\gamma$  is a free parameter determining the strength of the perturbation, and

$$\begin{aligned} B_x(t) &= \sum_{i=1}^3 A_{x,i} \sin(\omega_{x,i}t + \phi_{x,i}) \\ B_y(t) &= \sum_{i=1}^3 A_{y,i} \sin(\omega_{y,i}t + \phi_{y,i}) \\ B_z(t) &= \sum_{i=1}^3 A_{z,i} \sin(\omega_{z,i}t + \phi_{z,i}), \end{aligned} \quad (8)$$

where  $t$  is the time. The amplitudes  $A_{j,i}$  and the phases  $\phi_{j,i}$  are arbitrary fixed constants and remain unchanged for all simulations ( $j = x, y, z$ ). The frequencies are given through  $\omega_{j,i} = \delta\Omega_{j,i}$ , where  $\Omega_{j,i}$  are arbitrary, but not rationally dependent constants (to avoid resonances) as well.  $A_{j,i}$ ,  $\phi_{j,i}$  and  $\Omega_{j,i}$  lay down the form of the potential. Then, the amplitude and the frequency of the perturbation are controlled by two parameters, namely  $\gamma$  and  $\delta$ , respectively (Huber 2001).

The perturbations are a linear combination of stationary waves that do not inject momentum.

If our system represents a molecular cloud then a perturbation similar to those described above can be due to star clusters, clouds or other massive objects passing irregularly in the vicinity. Indeed such stochastic encounters must be quite frequent in galactic disks and we assume that the average time between two encounters is,

$$\tau_{\text{pert}} = \frac{1}{f_{\text{pert}}} \gtrsim \tau_{\text{dyn}}, \quad (9)$$

where  $f_{\text{pert}}$  is the mean frequency of the encounters and  $\tau_{\text{dyn}}$  is the dynamical time. Thus, these encounters can provide a continuous low frequency energy injection on large scales.

Such a low frequency forcing scheme induces at first ordered particle motions, which are transformed in the course of time to random thermal motion, due to gravitational particle interaction.

### 3.5. Self-Gravity, Repulsion and Force Computation

Interaction forces include self-gravity and repulsive forces whose strength can be adjusted by a parameter. Repulsive forces may be a result of sub-resolution processes such as star-formation or quantum degeneracy. The particle interaction potential reads,

$$\Phi_p(r) = -\frac{Gm}{\sqrt{r^2 + \epsilon^2}} \left( 1 - \xi \frac{\epsilon^2}{(r^2 + \epsilon^2)} \right), \quad (10)$$

where  $m$  is the particle mass and  $r$  is here the distance from the particle center. On larger scales ( $\gtrsim \epsilon$ ) the potential is a Plummer potential  $\Phi_{\text{Pl}}$  (Plummer 1911; Binney & Tremaine 1994). On small scales ( $\lesssim \epsilon$ ) the deviation from a Plummer potential and the strength of the repulsive force is determined by the parameter  $\xi$ . The interaction potential becomes for instance repulsive in the range  $|r| < \epsilon\sqrt{3\xi - 1}$  if  $\xi > 1/3$  (see Fig. 1). If  $\xi = 0$ ,  $\Phi_p = \Phi_{\text{Pl}}$  holds.

The interaction forces are computed on the Gravitor Beowulf Cluster<sup>1</sup> at the Geneva Observatory with a parallel tree code. This code is based on the Fortran Barnes & Hut (1986, 1989) tree algorithm, and has been efficiently parallelized for a Beowulf cluster. It is available on request.

The time-integration is the leap-frog algorithm with uniform time-step, which ensures the conservation of the

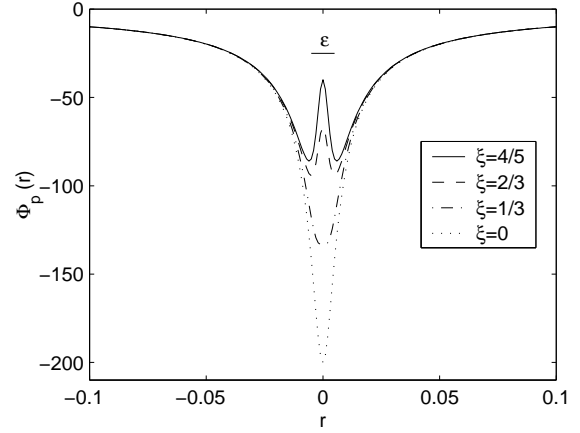


**Fig. 1.** The potential as a function of  $r$  in units of  $Gm/R$ , where  $m$  is the particle mass. A test particle at  $|r| < \epsilon\sqrt{3\xi - 1}$  feels a repulsive force if  $\xi > 1/3$ . The size of the softening parameter  $\epsilon$  is indicated, as well.

symplectic structure of the conservative dynamics. The time-step is,

$$\Delta t \leq 0.1 \frac{\epsilon}{\sigma_v}, \quad (11)$$

where  $\sigma_v$  is the velocity-dispersion of the initial state.

The accuracy of the force computation is given through the tolerance parameter, which is for the studies presented in this paper,  $\theta \leq 0.58$ .

### 3.6. Code Testing

In order to test the code, the evolution of the angular momentum is checked. We find that the angular momentum  $J$  of a system with 10000 particles and local dissipation scheme, which is initially  $J = 3.4 \times 10^{-5}$  in units such that energy is dimensionless, remains small,  $J < 4 \times 10^{-5}$ . This is illustrated by means of two examples. Two simulations with equal dissipation strength are carried out. One with short range repulsion,  $\xi = 2/3$ , and the other without,  $\xi = 0$ . After 10 crossing times the angular momentum is  $J = 3.3 \times 10^{-5}$  and  $J = 3.8 \times 10^{-5}$ , respectively. The deviation from the initial value is larger for the simulation without short range repulsion. This is because the dissipation leads in this case to a stronger mass concentration, i.e. to shorter particle distances. Indeed, the potential energy after 10 crossing times is  $U \approx -12$  and  $U \approx -17$  for the simulation with and without short range repulsion, respectively.

### 3.7. Parameters

The different dissipation schemes, the forcing scheme and the interaction potential with the short-distance repulsive force have several free parameters. In order to do a reasonably sized parameter study the particle number has to be limited to a maximum of  $N = 160000$ . However, im-

<sup>1</sup> <http://obswww.unige.ch/~pfenniger/gravitor/gravitor.html>

portant is not the absolute particle number, but the effect of changing it. Thus, also  $N$  is varied.

The model parameters and their ranges are indicated in Table 1.

#### 4. Correlation Analysis

In order to check if the perturbations of the gravitational system induce characteristic correlations in phase-space the indices  $D$  and  $\delta$  of the mass-size relation and the velocity-dispersion-size relation are determined.

The index of the mass-size relation can be found via,

$$D(r) = \left( \frac{d \log M}{d \log r} \right) (r), \quad (12)$$

where  $M$  is the sum of the masses of all particles having a relative distance  $r$ . The mass size relation is then

$$M(r) \propto r^{D(r)}, \quad (13)$$

where  $r$  can be considered as the scale. For a homogeneous mass distribution and for a hierarchical fragmented, fractal structure the index is a constant. For the latter case the index is not necessarily an integer and lies in the interval,  $D_T < D < D_S$ , where  $D_T$  and  $D_S$  are the topological dimension and the dimension of the embedding space, respectively (Mandelbrot 1982).

The index of the velocity-dispersion-size relation is determined by,

$$\delta(r) = \left( \frac{d \log \sigma}{d \log r} \right) (r), \quad (14)$$

where  $\sigma$  is the velocity-dispersion of all particles having a relative distance  $r$ . Observations of the interstellar medium suggest a constant index  $\delta = \delta_L$  on scales  $\mathcal{O}(0.1) - \mathcal{O}(100)$  pc with  $0.3 \lesssim \delta_L \lesssim 0.5$ . This is expressed by Larson's law (e.g. Larson 1981, Scalo 1985, Falgarone & Perault 1987, Myers & Goodman 1988)

$$\sigma \propto r^{\delta_L}. \quad (15)$$

In order to preclude the effect of boundary conditions on the scaling relations, upper and lower cutoffs have to be taken into account. The lower cutoff is given by the softening length. An upper cutoff arises from the final system size. Thus, the scope of application is for the velocity-dispersion-size and the mass-size relation,  $\epsilon < r < 2R_{90}$ , and  $\epsilon < r < R_{90}/2$ , respectively, where  $R_{90}$  is the radius of the sphere centered at the origin which contains 90% of the mass (see Huber & Pfenniger 2001a).

#### 5. Results: I. Properties of Equilibrium States in Numerical and Analytical Models

Here, some  $N$ -body gravo-thermal experiments of systems with weak dissipation, i.e., of systems in quasi-equilibrium are presented. The results are compared with theoretical findings.

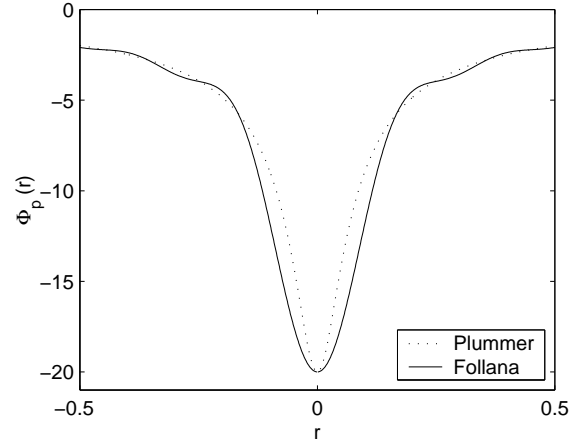


**Fig. 2.** The Follana ( $n = 10$ ) and the Plummer ( $\epsilon = 0.05$ ) potential, in units of  $Gm^2/R$ , where  $m$  is the particle mass.

In order to cover a range of energy with the same experiment, a convenient way is to introduce a weak global dissipation scheme allowing to describe a range of quasi-equilibrium states. Here weak means that  $\tau_{\text{dis}} \gg \tau_{\text{dyn}}$ , where  $\tau_{\text{dis}}$  is the dissipation time-scale. Then, the results can be compared with theoretical equilibrium states.

Follana & Laliena (2000) examined theoretically the thermodynamics of self-gravitating systems with softened potentials. They soften the Newtonian potential by keeping  $n$  terms of an expansion in spherical Bessel functions (hereafter such a regularized potential is called a Follana potential). This regularization allows the calculation of the thermodynamical quantities of a self-gravitating system. The form of their potential is similar to a Plummer potential with a corresponding softening length. Fig. 2 shows a softened Follana potential with  $n = 10$ , and a Plummer potential with  $\epsilon = 0.05$ .

In their theoretical work Follana & Laliena found for a mild enough regularization ( $n < 30$ ) a phase transition below the critical energy  $\epsilon_c \approx -0.335$  in a region with negative specific heat. The transition separates a high energy homogeneous phase from a low energy collapsed phase with core-halo structure.

We want to reproduce these findings by applying a Plummer potential ( $\xi = 0$ ). Furthermore, the effect of a small-scale repulsive force ( $\xi > 1/3$ ) is studied.

For these purposes, simulations with a weak global dissipation strength,  $\alpha = 0.025$ , are carried out. The dissipation time is then  $\tau_{\text{dis}} = 80 \tau_{\text{dyn}} = 56.6 \tau_{\text{ff}}$ , where the free fall time is,  $\tau_{\text{ff}} = \tau_{\text{dyn}}/\sqrt{2}$ .

Before we discuss the results, let us briefly present some model properties. The initial state is a relaxed, unperturbed and confined  $N$ -body sphere with total energy  $\epsilon = 1$ .

Assigning a particle a volume of  $4\pi\epsilon^3/3$ , the volume filling factor is,

$$V_{\text{ff}} = \frac{N\epsilon^3}{R^3}, \quad (16)$$

Parameter	Range	Description	Effect
$\delta$	$1/\tau_{\text{dyn}}, \dots, 2\pi/\tau_{\text{dyn}}$	Perturbation frequency	Perturbation potential
$\gamma$	$0, \dots, 0.7$	Perturbation factor	
$\Lambda$	$0, \dots, 5000$	Local dissipation factor	Local dissipation
$\lambda$	$2\epsilon, \dots, 50\epsilon$	Dissipation volume	
$\eta$	$0, 1, 2$	Relative distance power	
$\zeta$	$0, 1, 2$	Relative velocity power	
$\alpha$	$0, \dots, 50$	Global dissipation factor	Global dissipation
$\Gamma$	$0, \dots, 30$	Dynamical friction factor	Dynamical friction
$\epsilon$	$0.0046, 0.050$	Softening length	Interaction potential
$\xi$	$0, 1/3, 2/3, 1$	Repulsion strength	
$N$	$6400, \dots, 160000$	Particle number	Mass resolution

**Table 1.** Model parameters, characterizing energy injection (perturbation potential), dissipation, interaction potential (self-gravity and repulsion) and mass resolution.

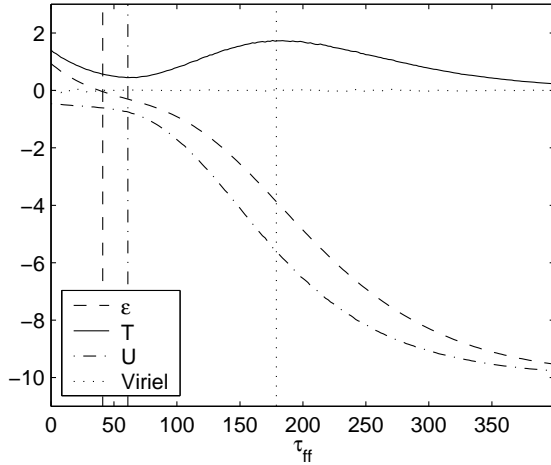


**Fig. 3.** The potential  $U$ , kinetic  $T$  and total energy  $\epsilon$  as a function of time for a simulation with global dissipation and Plummer softening ( $\xi = 0$ ). The temporal evolution of the virial equation is indicated as well ( $\text{Viriel} \equiv \ddot{I}/2$ ). The dashed vertical line depicts the time, when the system becomes fully self-gravitating. The dash-dotted and the dotted line mark the interval of negative specific heat.

where  $N$  is the particle number and  $R$  is the radius of the system. The volume filling factor is set  $V_{\text{ff}} = 1$ , meaning that the force resolution is equal to the mass resolution. Then, the particle number is,  $N = 8000$ .

The applied weak dissipation strength maintains the system approximately thermalized and virialized (see Fig. 3). Here a system of  $N$  particles is called virialized when the moment of inertia  $I$  is not accelerated,

$$\frac{\ddot{I}}{2} = 2T + \sum_{i=1}^N F_i r_i \approx 0, \quad (17)$$

where  $T$  is the kinetic energy,  $r_i$  is the location of the  $i$ -th particle and  $F_i$  is the sum of all forces acting on the particle (gravitation, friction, confinement).

The evolution of the inverse temperature  $\beta = 1/T$  as a function of the total energy  $\epsilon$  for two simulations with  $\xi = 0$  and  $\xi = 2/3$ , respectively, as well as the semi-

analytical curve calculated by Follana & Laliena are shown in the left panel of Fig. 4.

The interval of negative specific heat corresponds for the simulation with the Plummer potential with theoretical predictions. Also, in accordance with predictions, a phase transition takes place, separating a high energy homogeneous phase, from a collapsed phase in a interval with negative specific heat. Yet, the simulated phase transitions occur at higher energies. To illustrate this, the evolution of the Lagrangian radii  $\kappa$ , are shown in the middle and the right panel of Fig. 4.

In the high energy homogeneous phase the system is insensitive to the short-distance form of the potential. Thus all systems enter the interval of negative specific heat at the same energy. However, the collapsed phase is sensitive to the short-distance form. That is, the system with repulsive short-distance force reenters the interval of positive specific heat at a higher energy than those without such forces (see left panel of Fig. 4).

Furthermore, the collapsed phase resulting from a simulation with a Plummer potential is hotter and denser than those resulting from a simulation with repulsive small scale forces. This can be seen in Fig. 4 as well.

For a smaller softening length theory expects a phase transition at higher energies. Yet, already in simulations with a mild softening ( $\epsilon = 0.05$ ) the collapsing transition occurs straight after the system has entered the interval of negative specific heat, which is shortly after the system has become self-gravitating. Thus, the collapsing transition can not occur at significantly higher energies for a smaller softening length.

However, for systems with smaller softening length, the energy at which the system reenters the zone of positive specific heat after the collapse changes, i.e., it is shifted to smaller energies. This is shown in Fig. 5, where two simulations with  $N = 160000$  and  $\epsilon = 0.05$  resp.  $\epsilon = 0.01$  are compared.

Due to the higher particle number the dissipation time is in these simulations reduced to,  $\tau_{\text{dis}} = 4\tau_{\text{dyn}}$ . Thus, dynamical equilibrium is not as perfect as previously. That is, the acceleration of the moment of inertia  $I$  attains a maximum value of,  $\ddot{I}/T = 0.14$ , where  $T$  is the kinetic

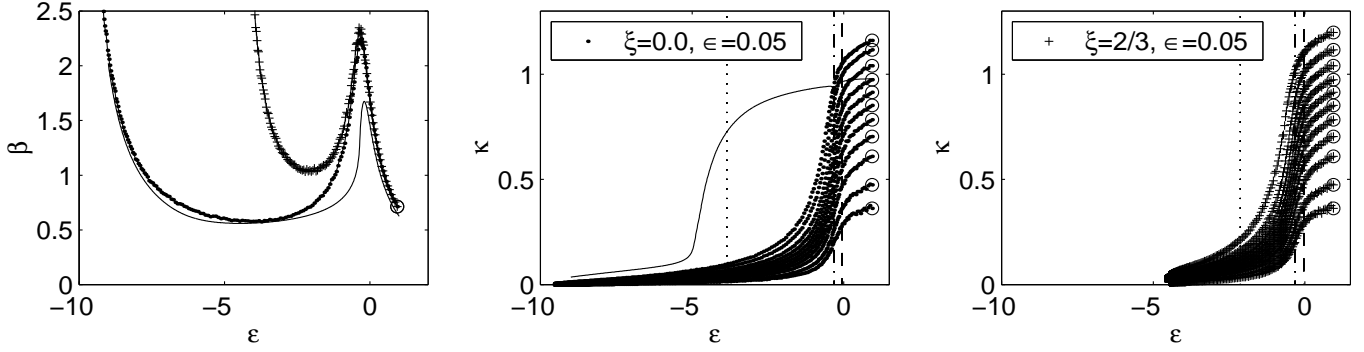


**Fig. 4.** Comparison of theoretical predictions and simulated systems. The simulations are carried out with  $N = 8000$  and the softening length is,  $\epsilon = 0.05$ . Consequently, the volume filling factor is,  $V_{\text{ff}} = 1$ . *Left:* Inverse temperature  $\beta$  versus energy  $\epsilon$  for models with softened potentials. The solid line indicates the theoretical result with the Follana potential,  $n = 10$ . The other curves depict the evolution of the simulated systems. Crosses: repulsive potential ( $\xi = 2/3$ ). Dots: Plummer potential ( $\xi = 0$ ). The circle indicates the initial state of the simulations. The range of negative specific heat corresponds to the range where the slope of  $\beta(\epsilon)$  is positive. *Middle:* The dotted lines describe the evolution of the Lagrangian radii  $\kappa$  for the simulation with the Plummer softening potential ( $\xi = 0$ ). Each curve depicts the radius of a sphere containing a certain mass fraction. The different mass fractions are:  $\Delta M/M = \{5\%, 10\%, 20\%, \dots, 80\%, 90\%, 95\%\}$ . The solid line depicts the theoretical 95%-Lagrangian radius for the Follana potential. The dashed vertical line depicts the moment when the system becomes fully self-gravitating. The dash-dotted and the dotted line mark the interval of negative specific heat. *Right:* Idem for the simulation with the short range repulsive force.

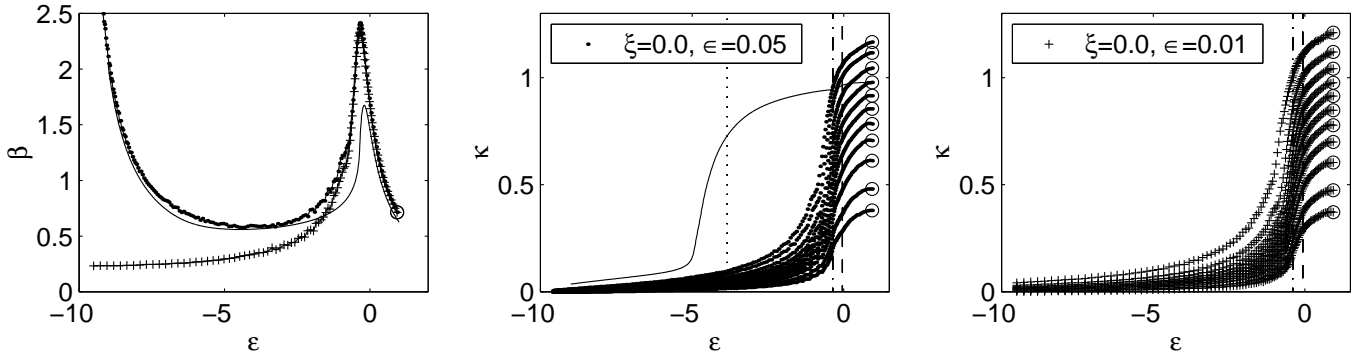


**Fig. 5.** Same as Fig. 4 for two simulations with  $N = 160000$  and with a Plummer potential  $\xi = 0.0$ . Dots:  $\epsilon = 0.05$ ,  $V_{\text{ff}} = 20.0$ . Crosses:  $\epsilon = 0.01$ ,  $V_{\text{ff}} = 0.16$ .

energy. However, in general dynamical equilibrium is well approximated and we expect, due to the experience with simulations with varying particle number and dissipation time, that the effect of the temporal deviation from equilibrium does not affect qualitatively the results presented in Fig. 5.

The volume filling factor of the systems with  $N = 160000$  and  $\epsilon = 0.05$  is,  $V_{\text{ff}} = 20$ , meaning that the mass resolution is a factor 2.7 larger than the force resolution. Thus the system is less granular than in the previous simulations with  $N = 8000$  and  $V_{\text{ff}} = 1$  (see Fig. 4). Yet, this does not affect the simulated quasi-equilibrium states and the deviation from theoretical predictions remains.

### 5.1. Discussion

Some predictions made by analytical models, such as the interval of negative specific heat, agree with findings resulting from  $N$ -body models. Yet, there appear also discrepancies, such as the way the collapsing phase transition develops.

At first sight the deviating results are surprising. Yet, the small scale physics is different in the two models which may account for the discrepancies. Indeed, thermostatics assumes a smooth density distribution and is thus not able to account for two-body relaxation effects in granular media. However, a certain degree of granularity is an inherent property of  $N$ -body systems. This may then lead to discrepancies, especially in the unstable interval of negative specific heat, where phase transitions may be sensitive to small scale physics.

Whereas thermostatics is too smooth to account for microscopic physics in granular self-gravitating media such as the interstellar gas, two-body relaxation is often too strong in  $N$ -body system due to computational limitations. Especially in high force resolution simulations where the force resolution is larger than the mass resolution. We refer to this in Sect. 6.1 where we discuss, among other things, the effect of the granularity on long-range correlations appearing in the interval of negative specific heat.

A further discrepancy between nature, analytical models and  $N$ -body models may be due to the entropy used in gravo-thermal statistics (Taruya & Sakagami 2001). Indeed, the entropy used in analytical models to find equilibrium states via the maximum entropy principle is the extensive Boltzmann-Gibbs entropy, that is in fact not applicable for non-extensive self-gravitating systems.

Generalized thermostatics including non-extensivity are currently developed (Tsallis 1988; Sumiyoshi 2001; Latora et al. 2001; Leubner 2001). These formalisms suggest that non-extensivity changes not all but some of the classical thermodynamical results (Tsallis 1999; Boghosian 1999), which agrees with our findings.

Because currently it is a priori not known which thermostatical properties change in non-extensive systems and consistent theoretical tools are not available, analytical results must be considered with caution.

## 6. Results: II. Transient Long-Range Correlations in Gravitational Collapses

### 6.1. Effect of Dissipation

Properties of equilibrium states differing from theoretical predictions in the interval of negative specific heat were found (see above). Let us, now study the nonlinear structure growth in this interval for an increased dissipation strength, i.e., outside of equilibrium, when  $\tau_{\text{dis}} \lesssim \tau_{\text{ff}}$ .

As previously, a relaxed, unperturbed, confined  $N$ -body sphere with  $\varepsilon = 1$  serves as initial state for the simulations.

In order to dissipate the energy different dissipation schemes are applied. Before we discuss the appearance of long-range correlations in unstable dissipative systems let us briefly discuss the effect of the different dissipation schemes on the global system structure.

The different applied dissipation schemes (see Sect. 3.3) lead to collapsed phases with different global structures. That is, they have different mass fractions contained in the core and the halo. A typical ordering is,  $\mathcal{D}_{\text{global}} > \mathcal{D}_{\text{dyn}} > \mathcal{D}_{\text{local}}$ , where,  $\mathcal{D}_{\text{global}}$ ,  $\mathcal{D}_{\text{dyn}}$  and  $\mathcal{D}_{\text{local}}$  are the density contrasts resulting from simulations with a global dissipation scheme, dynamical friction and a local dissipation scheme, respectively. The density contrast is,  $\mathcal{D} \equiv \log(\rho_{\text{cm}}/\rho_0)$ , where  $\rho_{\text{cm}}$  and  $\rho_0$  are the center of mass density and the peripheric density, respectively. This means that for a global dissipation scheme almost all the mass is concentrated in a dense core, whereas a local dissipation scheme can form a persistent “massive” halo.

The evolution of the mass distribution resulting from simulations with the different dissipation schemes is shown in Fig. 6. The collapse of the inner shells takes in all systems about the same time. Yet, the uncollapsed matter distributed in the halo is for the global dissipation scheme less than 2%, whereas it is 10% for the local dissipation scheme.

Next, temporary long-range correlations that develop in unforced gravitating systems are presented in dependence of the different system parameters.

A sufficiently strong global dissipation, i.e.,  $\tau_{\text{dis}} \lesssim \tau_{\text{ff}}$ , of a gravitating system leads during the nonlinear phase of the collapsing transition to fragmentation and long-range phase-space correlations, so that the index,  $\delta(r)$ , of the velocity-dispersion size relation,  $\sigma \propto r^{\delta(r)}$ , becomes positive.

Fig. 7 shows the evolution of the velocity-dispersion-size relation, i.e., of  $\delta$  for different dissipation strengths. The relations result from 3 different simulations with global dissipation schemes and different dissipation strengths. The dissipation strength is given through the parameter  $\alpha$ . Here  $\alpha = 1.0, 5.0, 9.0$ . This corresponds to  $\tau_{\text{dis}} = 2.0, 0.4, 0.2 \tau_{\text{ff}}$ .

Whereas the velocities remain uncorrelated in the simulation with  $\alpha = 1.0$ ,  $\delta$  becomes temporary positive over the whole dynamical range in the simulations with the stronger dissipation.

The velocity correlations start to develop at largest scales after the system has become self-gravitating. After the system has entered the interval of negative specific heat the correlation growth is accelerated. It attains a maximum and finally disappears when the collapse ends. The dynamical range over which  $\delta > 0$  during maximum correlation is  $\approx 2$  dex.

Correlations at small scales straight above the softening length are stronger for a stronger energy dissipation.

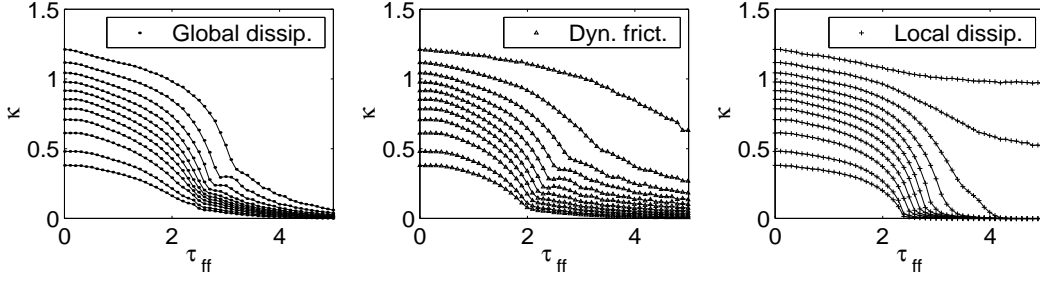
The maximum correlation established in the negative specific heat interval persists for  $\mathcal{O}(0.1) \tau_{\text{ff}}$  and is characteristic for the applied dissipation strength and softening. For instance, the simulation with the strongest dissipation develops during  $0.3 \tau_{\text{ff}}$  a roughly constant  $\delta$  over a range of 1.5 dex that resembles Larson’s relation. Yet, correlations at small scales decay rapidly and the index  $\delta$  becomes even negative at intermediate scales.

The end of the collapse and with it the disappearance of the correlated velocity structure is marked by a diverging negative specific heat  $c_V \rightarrow -\infty$ . This is shown in Fig. 8.

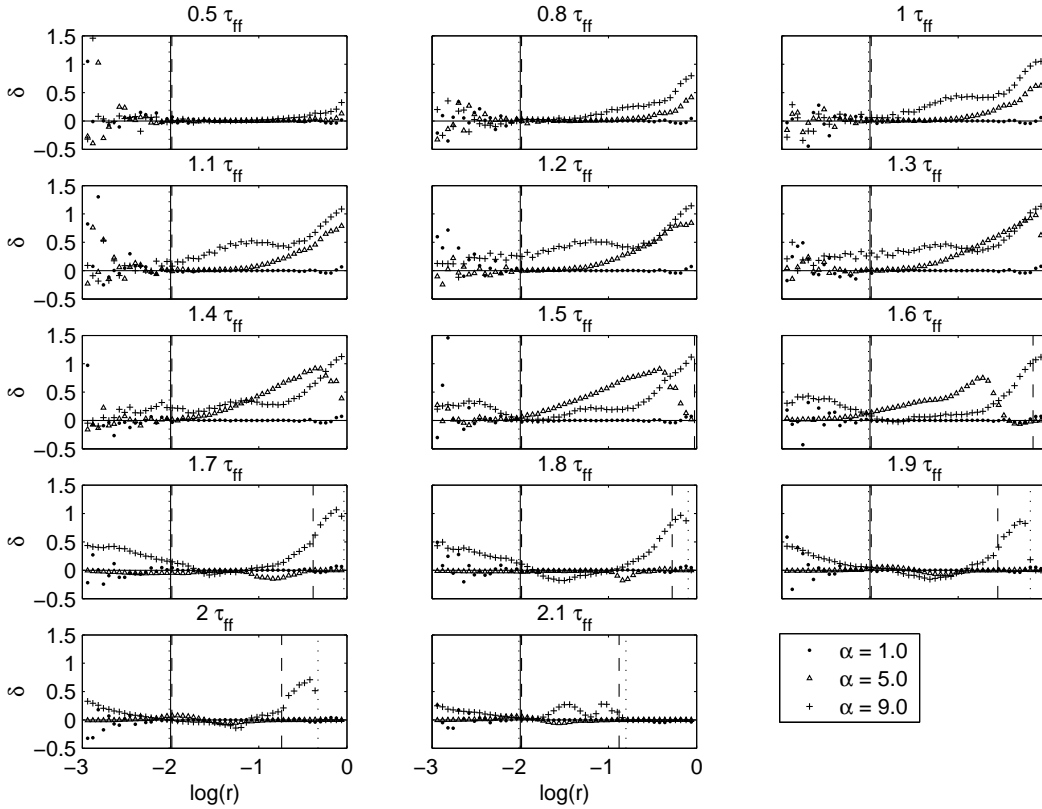
Systems with dynamical friction and local dissipation develop also velocity correlations.

Fig. 9 shows the correlations resulting from simulations with a local dissipation scheme. Contrary to the global dissipation scheme, a strong local dissipation does not extend the collapse of the whole system. Thus, local friction forces, that are strong enough to develop correlations lead also to a fast collapse and correlations persist accordingly a short time compared to simulations with global dissipation.





**Fig. 6.** Evolution of the Lagrangian radii for a system with global dissipation scheme, dynamical friction and a local dissipation scheme, respectively. The Lagrangian radii depict, here and in the following figures, spheres containing the following mass fractions:  $\Delta M/M = \{5\%, 10\%, 20\%, \dots, 80\%, 90\%, 98\%\}$ .



**Fig. 7.** Evolution of the index,  $\delta(r)$ , of the velocity-dispersion-size relation,  $\sigma \propto \delta(r)$ , during the collapsing transition for three simulations with **global** dissipation scheme and different dissipation strength. The correlations result from simulations that were carried out with 160000 particles. The solid, the dashed and the dotted vertical lines indicate the scope of application of the simulation with  $\alpha = 1.0$ ,  $\alpha = 5.0$  and  $\alpha = 9.0$ , respectively. The lower cutoff is given by the softening length, that is here  $\epsilon = 0.01$ , and the upper cutoff by  $2R_{90}$ . The time is indicated above each panel. The corresponding evolution of the Lagrangian radii and the specific heat are shown in Fig. 8.

The corresponding evolution of the Lagrangian radii and the interval of negative specific heat are shown in Fig. 10.

In the dynamical friction scheme, energy dissipation depends, as in the global dissipation scheme, on the absolute particle velocity. Thus a strong dynamical friction extends the gravitational collapse and the “lifetime” of the correlations. Yet, the observed phase-space correlations are weaker, compared to those appearing in simulations with global and local dissipation, respectively, mean-

ing that the reduced dissipation strength for fast particles, accordingly to the dynamical friction scheme, destroys the correlations.

## 6.2. Effect of Short Distance Regularization

So far the velocity correlations in dependence of the different dissipative factors were studied. Next the effect of different short distance regularizations of the Newtonian potential, removing its singularity, are checked. That is, sim-

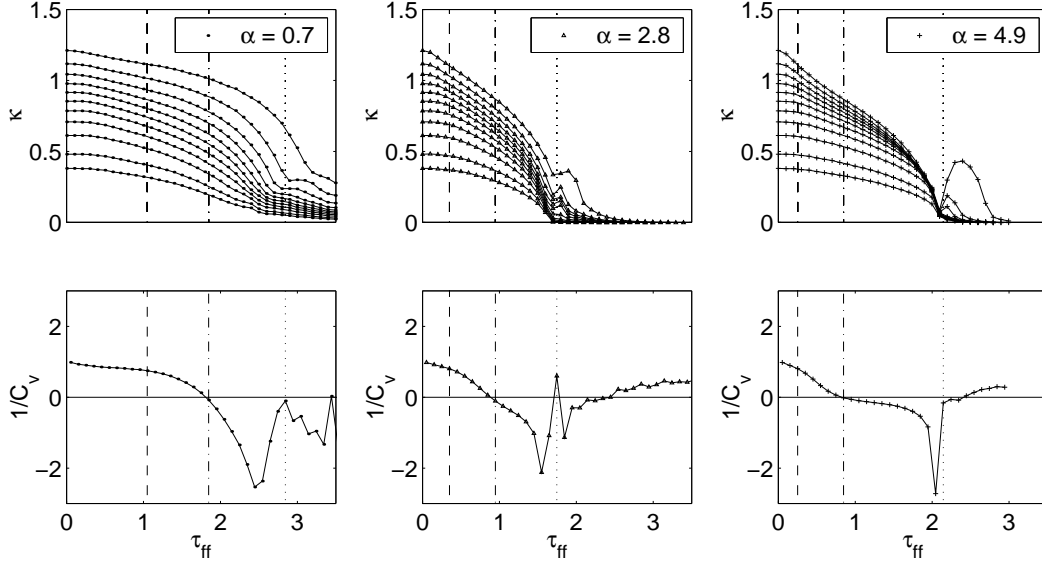


**Fig. 8.** Evolution of the Lagrangian radii (top) and the specific heat (bottom) for three simulations with **global** dissipation and different dissipation strength. The dashed line marks the moment, when the system becomes fully self-gravitating. The dash-dotted line indicates the moment when the system enters the zone of negative specific heat. The dotted line marks the “end” of the collapse. The evolution of the corresponding phase-space correlations are shown in Fig. 7.

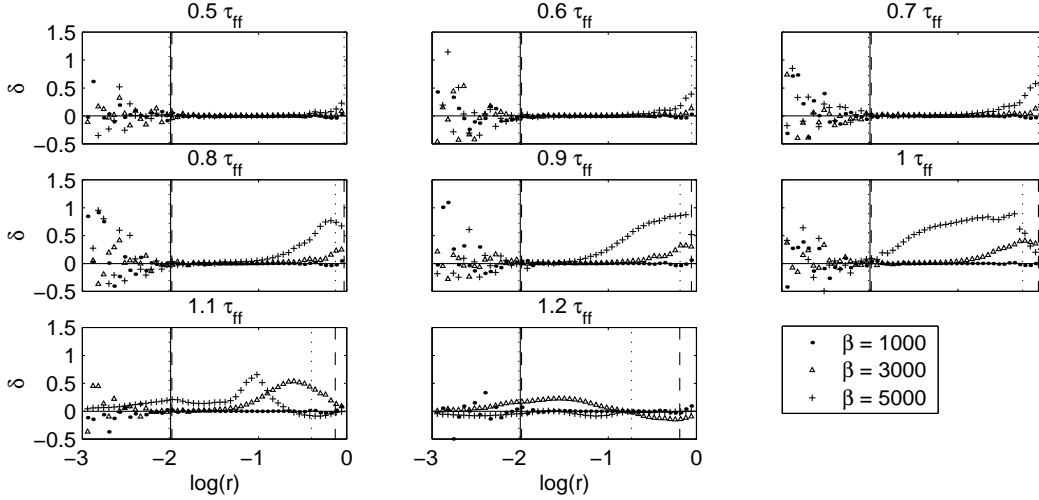


**Fig. 9.** Evolution of the index of the velocity-dispersion-size relation for three simulations with a **local** dissipation scheme and different dissipation strengths. The particle number is,  $N = 160000$ , and the softening length is,  $\epsilon = 0.01$ . The solid, the dashed and the dotted vertical lines indicate the scope of application of the simulation with  $\beta = 1000$ ,  $\beta = 2000$  and  $\beta = 5000$ , respectively. The parameters determining the dependence of the local dissipation on the radius and the velocity are,  $\eta = 1$  and  $\zeta = 1$ , respectively (see Sect 3.3.1). The evolution of the corresponding Lagrangian radii and the interval of negative specific heat are shown in Fig. 10.

ulations with and without short distance repulsive forces and with different dissipation strengths are carried out. Energy is dissipated via the global dissipation scheme.

In Fig. 11 the velocity correlations resulting from three simulations with three different regularizations are compared. The regularizations are characterized by two parameters. Namely, the softening length  $\epsilon$  and the parameter  $\xi$ , that determines the strength of the repulsive force. The softening length and  $\xi$  of the three sim-

ulations, compared in Fig. 11, are,  $(\epsilon = 0.01, \xi = 0.0)$ ,  $(\epsilon = 0.01, \xi = 2/3)$  and  $(\epsilon = 0.05, \xi = 0.0)$ , where  $\xi = 0.0$  means that a Plummer potential is applied and  $\xi > 1/3$  means that short distance repulsive forces are at work (see Sect. 3.5). The dissipation strength is for all three simulations the same,  $\alpha = 10$ , and the collapsing time is consequently the same as well (see Fig. 12).

During the first  $\tau_{ff}$  long-range correlations resulting from the three simulations are identical. Then the  $\delta(r)$

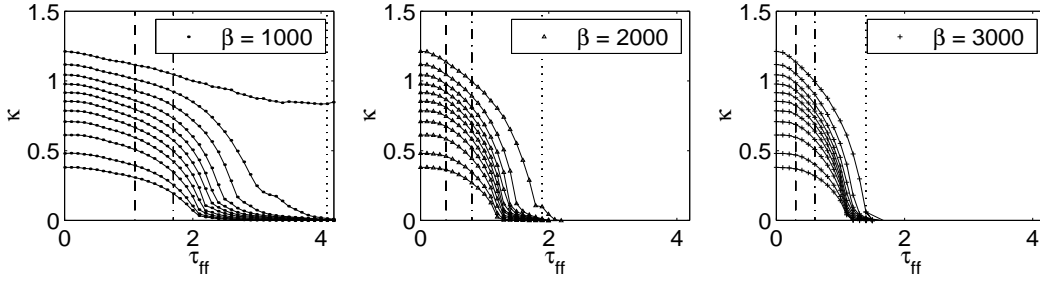


**Fig. 10.** Evolution of the Lagrangian radii and the specific heat for three simulations with **local** dissipation and different dissipation strength. The interval of negative specific heat is depicted by the dash-dotted and dotted line. The dashed line marks the moment when the whole system becomes self-gravitating. Fig. 9 shows the evolution of the corresponding long-range correlations.

starts to separate. Indeed, the repulsive forces cause an increase of  $\delta$  at small scales, compared to the simulation with the same softening length, but without repulsive forces. Yet, large scales remain unaffected.

The index  $\delta(r)$  resulting from the simulation with the large softening length is larger compared to the other two simulations after one  $\tau_{\text{ff}}$ . Also, the  $\delta(r)$  curve is flatter after that time.

The large difference between the simulation with the large softening length and the corresponding simulation with the small softening length is astonishing, because there is a clear deviation even at large scales. Well, the two simulations were carried out with the same particle number,  $N = 160000$ . Consequently, the volume filling factors are different. Namely,  $V_{\text{ff}} = 25$  and  $V_{\text{ff}} = 0.16$ , meaning that for the large softening length, i.e., the large  $V_{\text{ff}}$ , the mass resolution is larger than the force resolution and vice versa for the small softening length. Whereas a small volume filling factor describes a granular phase, a large volume filling factor describes rather a fluid phase. Thus the deviation of the velocity correlations may mainly be due to the different volume filling factors and not due to the different softening lengths.

In order to check this some complementary numerical experiments are carried out, whose results are presented subsequently.

### 6.3. Granular and Fluid Phase

The upper panels in Fig. 13 show the velocity-dispersion-size relation, that develop in simulations with different volume filling factors, but equal softening length,  $\epsilon = 0.031$ . The particle numbers are,  $N = 6400$ ,  $N = 32000$  and  $N = 160000$ . Thus, the volume filling factors are,  $V_{\text{ff}} = 0.2$ ,  $V_{\text{ff}} = 1.0$  and  $V_{\text{ff}} = 5.0$ , respectively. Strongest phase-space correlations appear in the simulation with the highest mass resolution, i.e., for the “fluid phase”, and weakest correlations appear in the “granular phase”. The flattest  $\delta(r)$  curve results from the simulation in which force and mass resolution are equal.

This result suggests that the volume filling factor  $V_{\text{ff}}$  (and not the softening length) is the crucial parameter

determining the correlation strength in simulations with equal dissipation strength, as long as a substantial part of the system forces stem from interactions of particles with relative distances larger than the softening length.

The lower panels in Fig. 13 show, for the same simulations, the evolution of the index,  $D(r)$ , of the mass-size relation,  $M \propto r^{D(r)}$ . The deviation from homogeneity is strongest for the “granular phase” and weakest for the “fluid phase”. Thus the order of the correlation strength in space is inverse to the order of the correlation strength in phase-space. Such an inverse order is expected in self-gravitating system with  $|U| \propto T$ , where  $U$  is the potential energy and  $T$  is the kinetic energy (Pfenniger & Combes 1994; Pfenniger 1996; Combes 1999).

The corresponding Lagrangian radii and the interval of negative specific heat are shown in Fig. 14.

### 6.4. Initial Noise

Assuming a constant softening length, different volume filling factors,  $V_{\text{ff}}$ , mean different particle numbers,  $N$ , that introduce different Poisson noise,  $\sim \sqrt{N}$ . Then, the statistical roughness of the initial uniform Poisson particle distribution decreases like  $\sim 1/\sqrt{N}$ .

Thus the initial roughness of the latter simulations (see Fig. 13) differ from each other by a factor  $\sim 2.2$  and one might suppose that the different correlation strengths in these simulations are the result of the different statistical, initial roughness.

In order to check this possibility, long-range correlations are compared that result from two simulations with  $V_{\text{ff}} = 1.0$  and with statistical roughness that differs by a factor  $\sim 2.2$ . The results are presented in Fig. 15 and the corresponding Lagrangian radii are shown in Fig. 16. The simulation with  $N = 32000$  was already presented in Fig. 13. It is now compared with a simulation with stronger initial roughness.

Despite the different initial roughness, long-range correlations in phase-space are almost identical for the two simulations.

As regards fragmentation, additionally to the parameter of the mass-size relation, the mass distribution in space

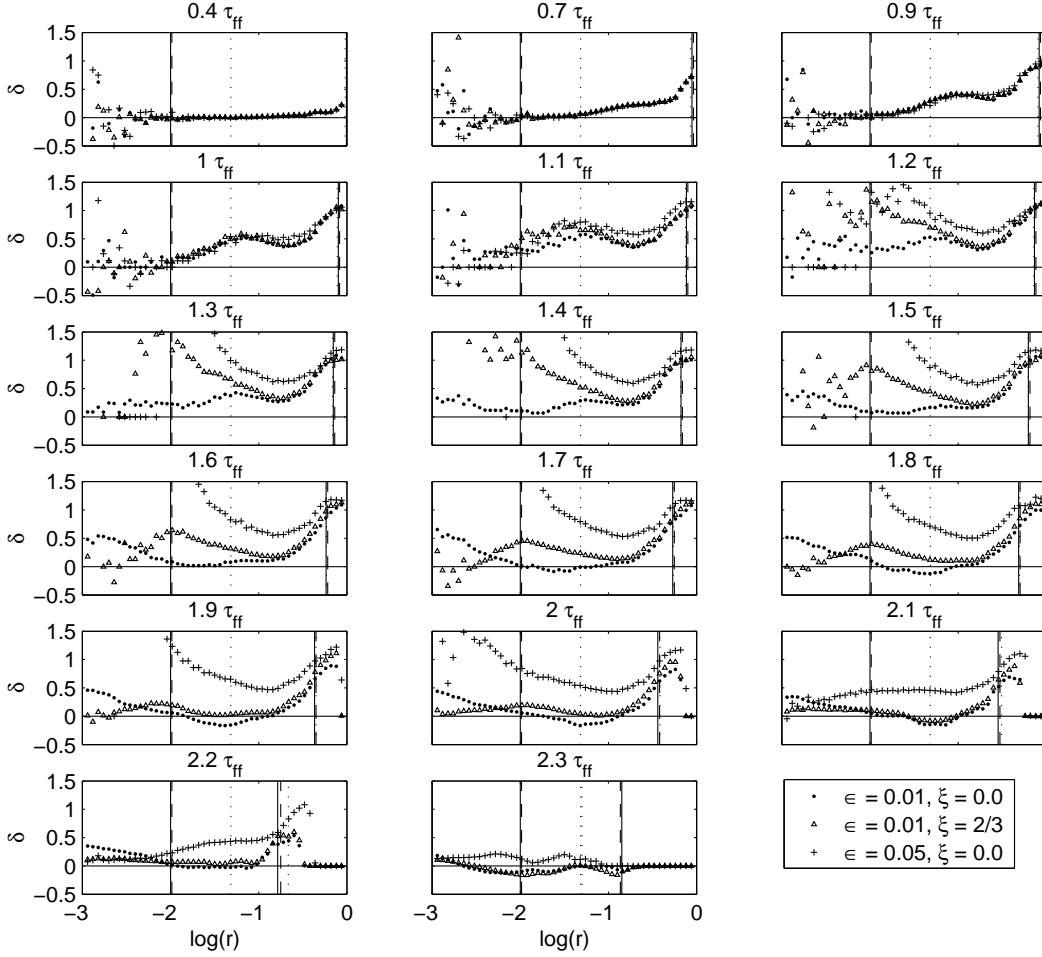


**Fig. 11.** Evolution of the velocity correlations for three simulations with global dissipation scheme and different **potential regularizations**. That is, the softening length and the form of the softening, respectively, change from simulation to simulation. For  $\xi = 0.0$  the particle potential is a Plummer.  $\xi = 2/3$  means that there are short distance repulsive forces at work. The particle number is,  $N=160000$ . The solid, the dashed and the dotted vertical lines indicate the scope of application of the simulation with  $(\epsilon = 0.01, \xi = 0.0)$ ,  $(\epsilon = 0.01, \xi = 2/3)$  and  $(\epsilon = 0.05, \xi = 0.0)$ , respectively. The evolution of the corresponding Lagrangian radii are shown in Fig. 12.

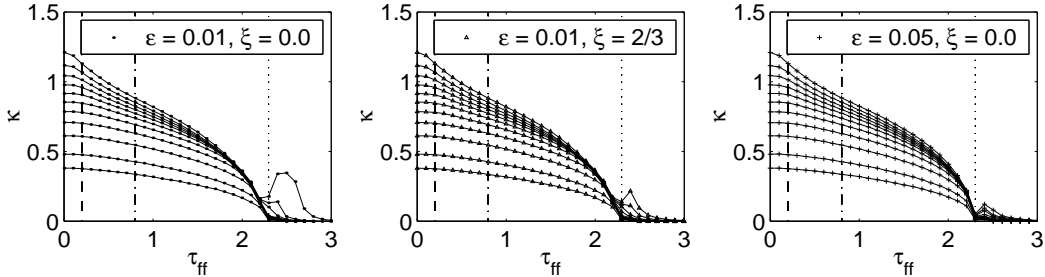


**Fig. 12.** Same as Fig. 10 for three simulations with different **potential regularizations**, i.e., different softening lengths and forms of the softening potential, respectively. The evolution of the corresponding phase-space correlations are shown in Fig. 11.

were compared. We find actually a stronger fragmentation for small particle numbers. Yet, the  $V_{ff}$  seems to be the crucial parameter for the fragmentation strength in Fig. 13.

Consequently, the different correlation strengths in Fig. 13 can not be accounted for by Poisson noise, but are

mainly the result of the different volume filling factors, or more precisely, due to the different ratio of force and mass resolution. Thus dark matter clustering in high-resolution cosmological  $N$ -body simulations in which the force resolution is typically an order of magnitude smaller than

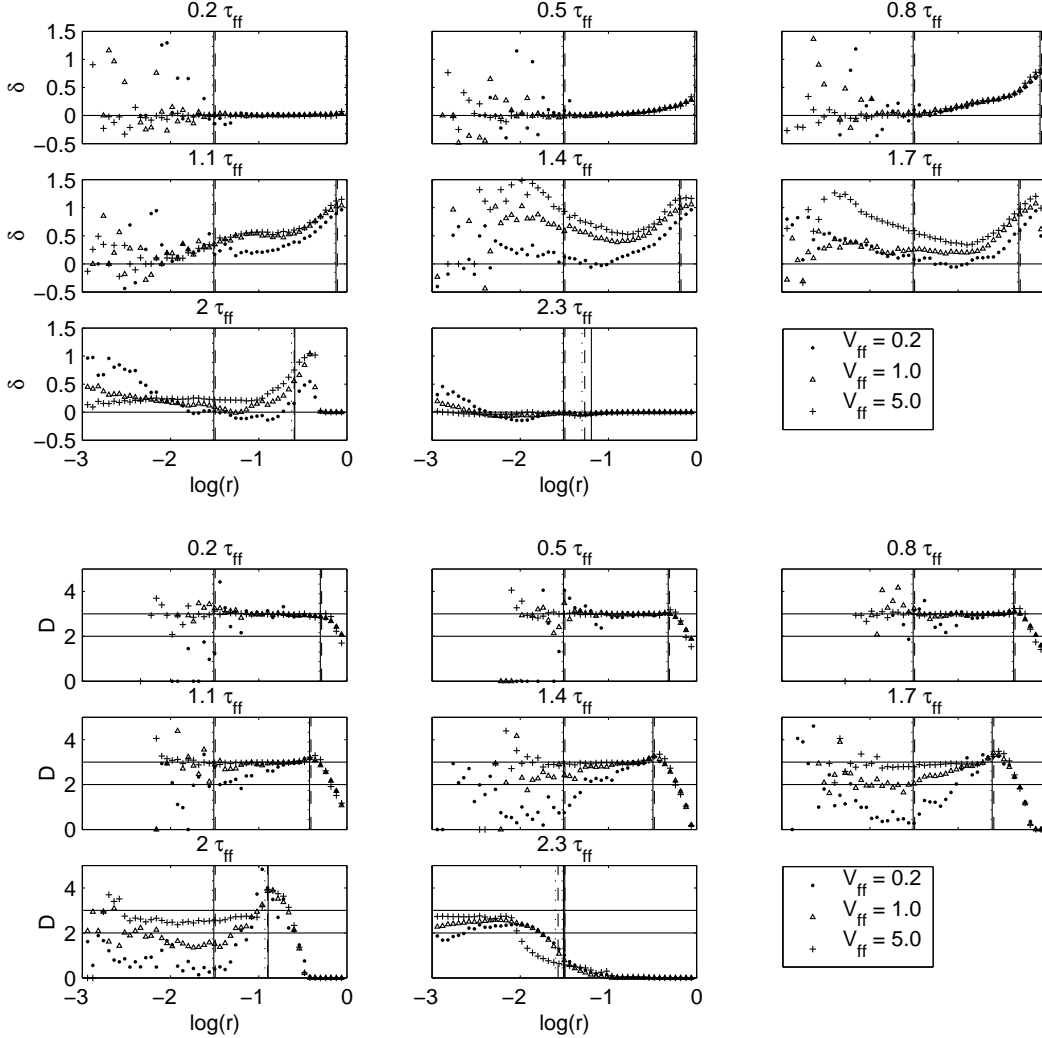


**Fig. 13.** *Upper panels:* Evolution of the index,  $\delta(r)$ , of the velocity-dispersion-size relation,  $\sigma \propto r^{\delta(r)}$ , resulting from three simulations with different **volume filling factor** that describe a granular phase,  $V_{ff} = 0.2$ , a fluid phase,  $V_{ff} = 5.0$ , and an intermediate state,  $V_{ff} = 1.0$ . The particle numbers are  $N = 6400$ ,  $N = 160000$  and  $N = 32000$ , respectively. The softening length is  $\epsilon = 0.031$ . The solid, the dashed and the dotted vertical lines indicate the scope of application of the simulation with  $V_{ff} = 0.2$ ,  $V_{ff} = 1.0$  and  $V_{ff} = 5.0$ , respectively. The scope is given by,  $\epsilon < r < 2R_{90}$ . The corresponding Lagrangian radii are presented in Fig. 14. *Lower panels:* The evolution of the index,  $D(r)$ , of the mass-size relation,  $M \propto r^{D(r)}$ . The solid, the dashed and the dotted vertical lines indicate the scope of application of the simulation with  $V_{ff} = 0.2$ ,  $V_{ff} = 1.0$  and  $V_{ff} = 5.0$ , respectively. The scope is given by,  $\epsilon < r < R_{90}/2$ .

the mass resolution may be too strong compared with the physics of the system (Hamana et al. 2001).

### 6.5. Free Fall of Cold Dissipationless Systems

Here, long-range correlations are discussed that develop in cold, gravitationally unstable systems without energy dissipation. The correlations strength appearing in such dissipationless systems depends on the initial ratio between kinetic and potential energy,  $a = T/|U|$ , i.e., on the number of thermal Jeans masses given through  $M/M_J = 2a^{-3/2}$ .

This is shown in Fig. 17. For  $a = 0.01$  the index  $\delta$  of the velocity-dispersion-size relation remains zero at small scales during the whole free fall, whereas for  $a = 0.0$  the

index becomes,  $\delta > 0$ , over the whole dynamical range, during a period of  $\sim 0.7\tau_{ff}$ . That is,  $350 M_J$  are not sufficient to develop small scale phase-space correlations in a dissipationless system.

In order to show the dependence of the result on the initial Poisson noise, the absolutely cold simulation with  $N = 160000$  is compared with a  $N = 32000$ -body simulation. As above, it follows that the initial roughness of the two systems differs by a factor  $\sim 2.2$ .

Fig. 17 shows that the non-equilibrium structures resulting from the simulations with equal  $a$  but unequal particle number differ from each other during the whole free fall. Indeed, during the first half of the free fall time the two initial conditions produce velocity correlations that differ on small and large scales. After  $t = 0.5 \tau_{ff}$  the dif-

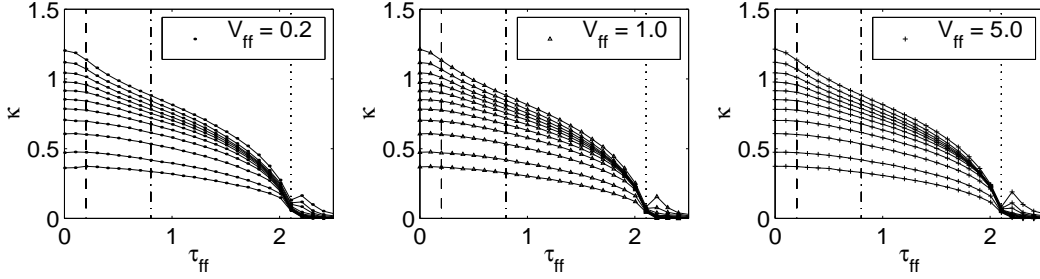


**Fig. 14.** Same as Fig. 10 for three simulations with different **volume filling factor**. Fig. 13 shows the evolution of the corresponding long-range correlations.

ferences approximately disappear. However, the behavior of the spatial correlations (see lower panels of Fig. 17) is inverse, meaning that differing spatial correlations appear after  $0.5 \tau_{\text{ff}}$  and persist for the rest of the free fall.

These results suggest that non-equilibrium structures appearing in cold systems or in systems with very effective energy dissipation depend more strongly on initial noise than those appearing in warm systems with less effective dissipation (see also Fig. 15).

The evolution of the Lagrangian radii during the free fall of the cold, dissipationless systems are shown in Fig. 18. Because these systems are adiabatic and self-gravitating during the whole simulation, the corresponding intervals are not plotted in the figure.

## 6.6. Discussion

Long-range spatial and phase-space correlations appear naturally during the collapsing phase transition in the interval of negative specific heat if the energy dissipation time is,  $\tau_{\text{dis}} \lesssim \tau_{\text{ff}}$ , so that the time-scale of correlation growth is smaller than the time-scale of chaotic mixing which is,  $\sim 1/\lambda \propto \tau_{\text{ff}}$ , where  $\lambda$  is the maximum Liapunov exponent (Miller 1994).

Actually, the details of the long-range correlations depend on the applied dissipation scheme, but there are also some generic properties. That is, phase space correlations start to grow at large scales, whereas spatial correlations seem to grow bottom-up. Moreover, there is an upper limit for the index of the velocity-dispersion-size relation within the dynamical range, namely,  $\delta \approx 1$ .

Besides, the dissipation strength, and initial conditions, the volume filling factor  $V_{\text{ff}}$  is a crucial parameter for the correlation strength. That is, phase-space correlations are strong in the fluid limit and weak for a granular phase. The behavior of the spatial correlations is exactly the other way around.

The softening length does not affect correlations within the dynamical range. Yet, sub-resolution repulsive forces affect correlations on small scales above the resolution scale. Of course, this does not hold for the onset of the correlation growth, but only after sufficient particles have attained sub-resolution distances.

The above considerations suggest that the found correlations are physically relevant and not a numerical artifact.

The long-range spatial and phase-space correlations appearing during the collapsing transition are qualitatively similar to the mass-size and the velocity-dispersion-size relation observed in the ISM (e.g. Blitz & Williams 1999; Chappell & Scalo 2001; Fuller & Myers 1992), showing that in the models gravity alone can account for ISM-like correlations.

Furthermore, the time-scale of the correlation lifetime is the free fall time,  $\tau_{\text{ff}}$ , which is consistent with a dynamical scenario in which ISM-structures are highly transient (Vázquez-Semadeni 2002; Larson 2001; Klessen et al. 2000), which is related with rapid star formation and short molecular cloud lifetimes (Elmegreen 2000), that is, the corresponding time-scales are about an order of magnitude smaller than in the classical Blitz & Shu (1980) picture.

## 7. Results: III. Permanent Energy-Flow

### 7.1. Nonequilibrium Structures in Systems Subject to an Energy Flow

The numerical experiments presented above showed that dissipative self-gravitating systems fragment and establish long-range correlations outside of equilibrium in the interval of negative specific heat. These transient correlations persist for  $1 - 2 \tau_{\text{ff}}$  times.

Here we check if self-gravitating systems can establish persistent long-range correlations if they are maintained continuously outside of equilibrium by a permanent energy-flow. That is, the dissipated energy is continuously replenished by time-dependent potential perturbations.

Both simulations of granular and fluid phases are carried out. A typical parameter set, describing a granular system is,  $N = 10000$ ,  $\epsilon = 0.0046$ ,  $V_{\text{ff}} = 0.001$  and  $N = 160000$ ,  $\epsilon = 0.0315$ ,  $V_{\text{ff}} = 5$  are here typical for a fluid phase. Yet, the parameters are not fixed and the effect on the evolution is studied when parameters change. Parameters, controlling energy-flow and interaction potential, as well as their ranges are indicated in Table 1.

The applied potential perturbations imitate massive objects passing in the vicinity on time-scales,  $\tau_{\text{pert}} \lesssim \tau_{\text{dyn}}$ .

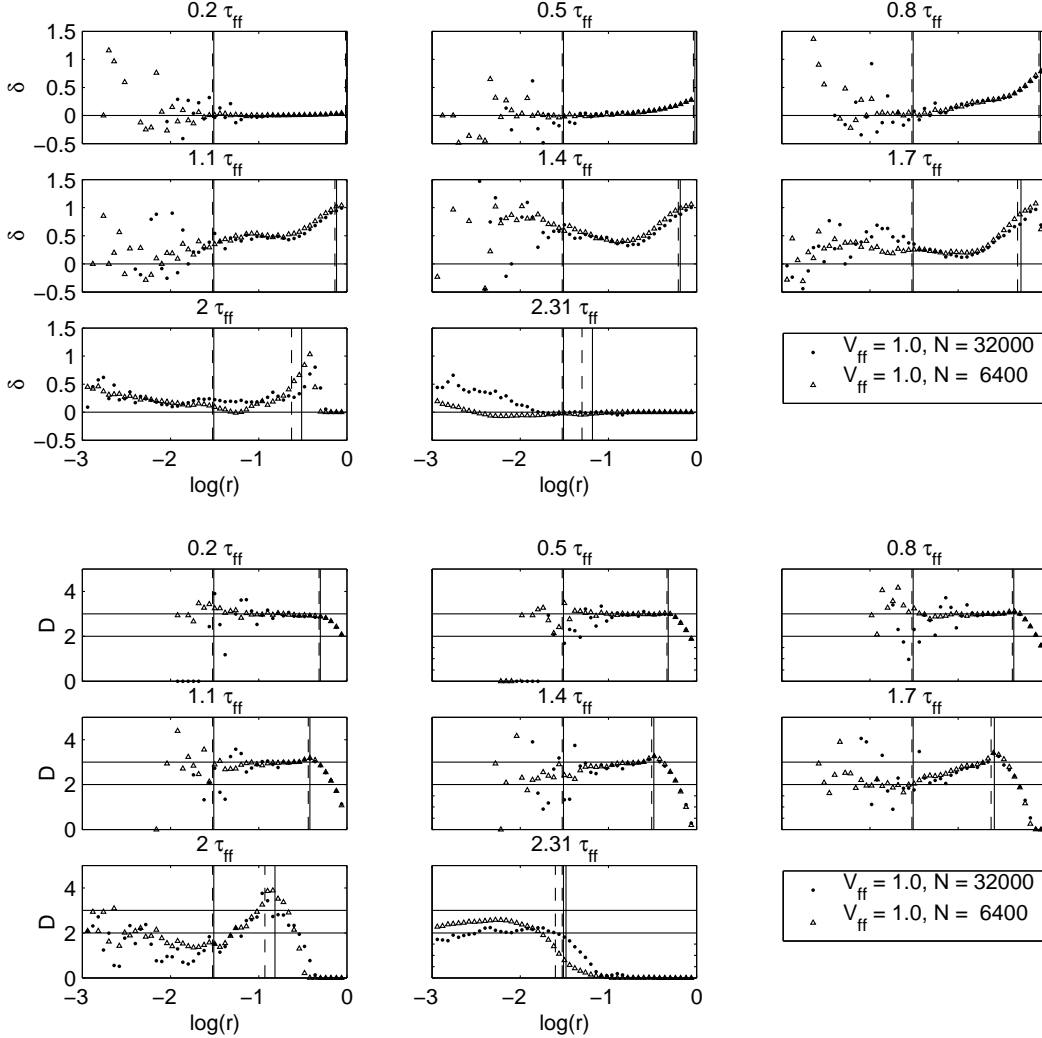


**Fig. 15.** *Upper panels:* Evolution of the phase-space correlations resulting, resulting from two simulations with identical volume filling factor,  $V_{\text{ff}} = 1.0$ , but unequal statistical, **initial roughness**,  $\sim 1/\sqrt{N}$ . The particle number and the softening length of the first simulation (dots) are  $N = 32000$  and  $\epsilon = 0.031$ , respectively. The second simulation (triangles) is carried out with  $N = 6400$  and  $\epsilon = 0.054$ . The solid and the dashed lines indicate the scope of application given by  $\epsilon < r < 2R_{90}$ . The evolution of the corresponding Lagrangian radii is shown in Fig. 16. *Lower panels:* The evolution of the spatial correlations. The scopes of application, depicted by the vertical lines, is,  $\epsilon < r < R_{90}/2$ .

The perturbations induce primarily ordered particle motions. Then gravitational interactions lead to a conversion of the bulk kinetic energy to random thermal motion. The energy injection due to such a forcing scheme can be quite regular until a plateau is reached.

Energy injection prevents a system from collapsing and maintains an approximately statistically steady state during  $\sim 5 - 15 \tau_{\text{dyn}}$  when energy dissipation is balanced appropriately by large scale potential perturbations. These states do not feature any persistent long-range correlations. Yet, they develop a temperature structure that is characteristic for the applied dissipation scheme. This is shown in Fig. 19, where the evolution of two granular systems subjected to an energy-flow is presented. One system dissipates its energy by a global dissipation scheme (top), the other by a local dissipation scheme (bottom).

The system with the global dissipation scheme is nearly thermalized during almost the whole simulation, whereas the local dissipation scheme leads to a permanent positive temperature gradient, that is inverse compared to stars and resembles those of the ISM where dense, cool mass condensation are embedded in hotter shells.

If dissipation dominates energy injection the system undergoes in general a mono-collapse, that is, a collapsed structure is formed in which a part of the system mass is concentrated in a single dense core and the rest is distributed in a diffuse halo. However, systems with a rather fluid phase may develop several dense cores moving in a diffuse halo, when they are subjected to an appropriate energy flow. In the course of time the number of clumps varies, but a non-mono-clump structure persists for some  $\tau_{\text{ff}}$  (see Fig. 20). These systems may even develop persistent phase-space correlations (see Fig. 21).

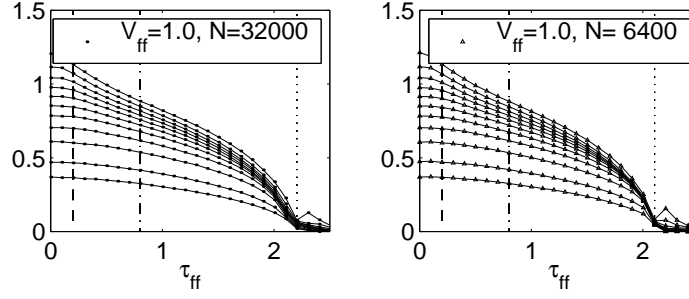


**Fig. 16.** Same as Fig. 10 for two simulations with identical volume filling factor and unequal **initial roughness**,  $\sim 1/\sqrt{N}$ . The evolution of the corresponding long-range correlations is shown in Fig. 15

However, the clumps result not from a hierarchical fragmentation process, but they are formed sequentially on the free fall time scale. Furthermore, the clumps are so dense that their evolution is strongly influenced by the applied regularization. That is, the evolution over several  $\tau_{\text{ff}}$  depend on the numerical model that does not represent accurately small-scale physics.

In order to impede gravitational runaway that may hinder the formation of complex non-equilibrium structures within the given dynamical range, different measures are taken, such as short distance repulsion and the application of the dynamical friction scheme, where the friction force  $F \rightarrow 0$  for  $v \rightarrow \infty$ .

Yet, despite these measure, we only find either nearly homogeneous structures in systems where energy injection prevails, or systems dominated by unphysical clumps in case of prevailing energy dissipation.

Up to now, mainly the effect of several different dissipation schemes were discussed. However, the effect of a modified forcing scheme is also checked. That is, a power-law forcing scheme is applied, which injects energy at different frequencies. This forcing scheme is a modification of those presented in Sect. 3.4 and reads,  $\Phi_{\text{pert}}(\omega) \propto \omega^\nu$ , where  $\nu = -4, \dots, 4$ . Yet, also such a forcing scheme can not induce a phase transition to complex non-equilibrium structures and the resulting mass distribution corresponds to the those described above.

## 7.2. Discussion

Actually the “clumpy” structure in Fig. 20 and the corresponding phase-space correlations shown in Fig. 21 do not represent real physics, nevertheless, they show that it is principally possible to maintain spatial non-equilibrium structures and long-range phase-space correlations in a perturbed, dissipative, self-gravitating system over several dynamical times. Thus, it can not be excluded that in the future, with a better representation of microscopic physics and forcing mechanisms at work in the ISM, models including self-gravity may produce complex nonhomogeneous structures in a statistical equilibrium, i.e., persistent patterns formed by transient structures.

However, at present models of dissipative, self-gravitating systems, cannot produce such structures on

the scale of Giant Molecular Clouds (e.g. Semelin & Combes 2000, Klessen et al. 2000, Huber & Pfenniger 2001a).

On larger scales, gravity gives rise to persistent non-equilibrium structures in cosmological and shearing box simulations. A common denominator of these models is that their time dependent boundary conditions are given by a scale-free spatial flow counteracting gravity. Let us discuss this more precisely.

In cosmological and shearing box models time-dependent boundary conditions create relative particle velocities that are inverse to gravitational acceleration and increase with particle distance,  $v \propto r$ . In the shearing box model, the relative azimuthal particle velocity due to the shear flow is,  $v_\theta \propto r_c$ , where  $r_c$  is the radial particle distance in cylinder coordinates. In cosmological models, the relative particle velocity induced by the Hubble flow is,  $v_r \propto r$ , where  $r$  is the relative particle distance in Cartesian coordinates.

These relations and consequently the corresponding flows are scale-free. The fact that the shear flow affects only the azimuthal velocity component may then account for the characteristic spiral arm like structures found in shearing box experiments, differing from those found in cosmological models, where the isotropic Hubble flow gives rise to in average isotropic non-equilibrium structures.

The models studied in this paper are not subject to a scale-free spatial flow counteracting gravity and persistent long-range correlations of astrophysical relevance do not appear. This may suggest that in situations where gravitational runaway is allowed, matter that has passed through a collapsing transition, has to be replenished at large scales in order to attain a statistical equilibrium state of transient fragmentation.

## 8. Conclusions

First, equilibrium states of  $N$ -body models were compared with analytical models. Subsequently, the findings resulting from this comparison are summarized:

- On the one hand, equilibrium properties of  $N$ -body models agree with predictions made by analytical models. An example is the energy interval of negative



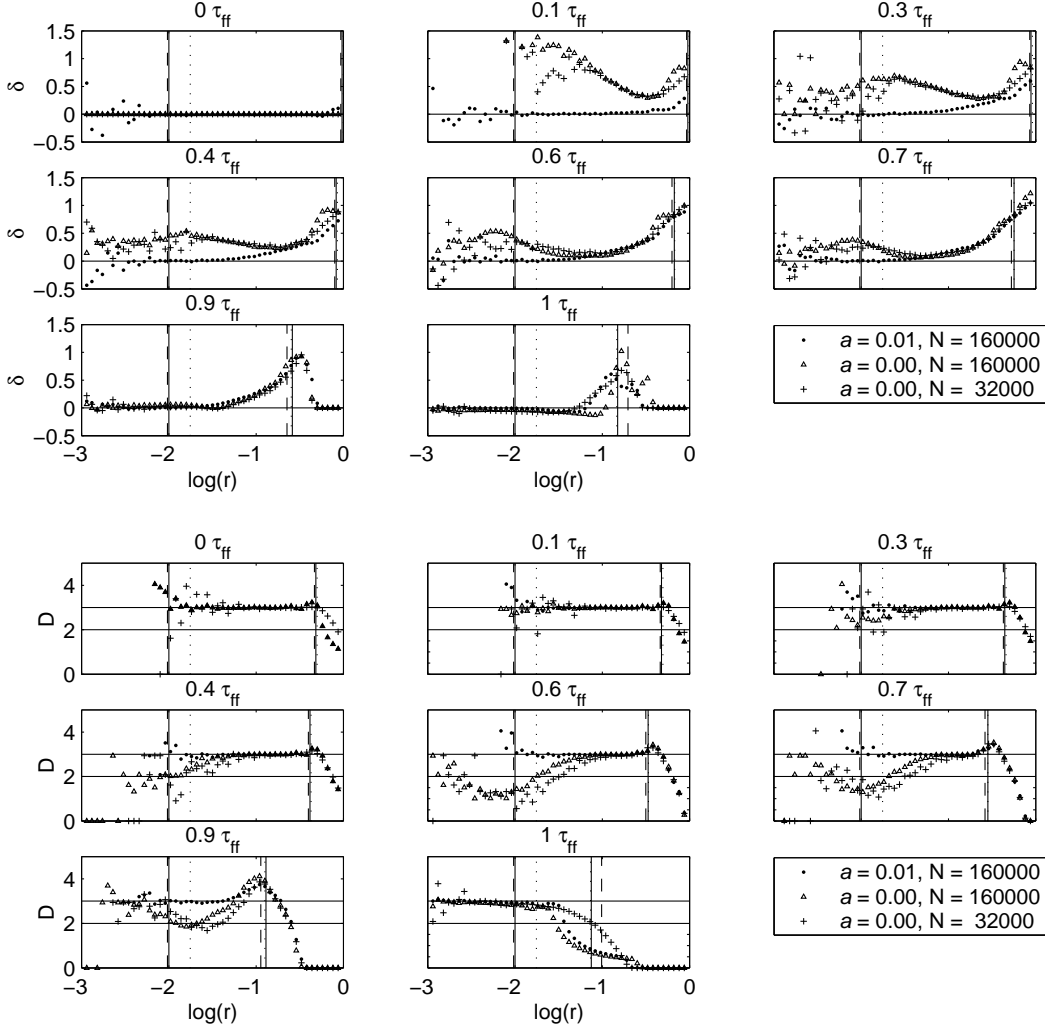


**Fig. 17.** *Upper panels:* Phase-space correlations that develop during the **free fall** of three cold, dissipationless systems. All systems have the same volume filling factor,  $V_{\text{ff}} = 0.016$ . The parameter  $a$  indicates the ratio between kinetic and potential energy. The solid, the dashed and the dotted lines indicate the scope of application,  $\epsilon < r < 2R_{90}$ , of the simulation with  $(a = 0.01, N = 160000)$ ,  $(a = 0.0, N = 160000)$  and  $(a = 0.0, N = 32000)$ , respectively. The evolution of the corresponding Lagrangian radii is shown in Fig. 18. *Lower panels:* Evolution of the spatial correlations. The scopes of application, depicted by the vertical lines, is,  $\epsilon < r < R_{90}/2$ .

specific heat. On the other hand, discrepancies were found, such as the way the collapsing phase transition, separating a high-energy homogeneous phase from a low-energy collapsed phase, develops in the interval of negative specific heat. These discrepancies suggest: 1.) Small scale physics becomes relevant for the system evolution when the growth of singularities triggered by gravitational instabilities is allowed. 2.) Analytical models based on the Gibbs-Boltzmann entropy are not strictly applicable to non-extensive self-gravitating systems. Yet, not all of the equilibrium properties found by maximizing the Gibbs-Boltzmann entropy are expected to change if a fully consistent, generalized thermostistical theory is applied.

Second, the collapsing transition was studied in systems with strong dissipation. The findings are:

- Dissipative self-gravitating systems develop outside of equilibrium, in the interval of negative specific heat, transient long-range correlations. That is, fragmentation and nonequilibrium velocity-dispersion-size relations, with striking resemblance to those observed in the ISM, appear during the collapsing transition, when the dissipation time is shorter than the dynamical time. This suggests that nonequilibrium structures in self-gravitating interstellar gas are *dynamical and highly transient*.
- Besides the dissipation strength and the initial noise, the granularity turns out to be a crucial parameter for the strength of the resulting long-range correlations, substantiating the importance of a coherent mass and force resolution. That is, phase-space correlations are stronger in the fluid limit than in a granular phase. The opposite holds for spatial correlations. This substanti-

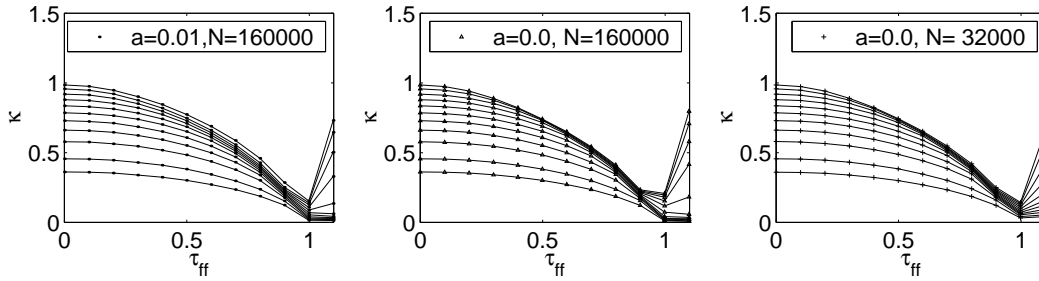


**Fig. 18.** Same as Fig. 10 for the **free fall** of three cold, dissipationless systems with identical volume filling factor but unequal  $a$  and initial roughness, respectively. The evolution of the corresponding long-range correlations is shown in Fig. 17.

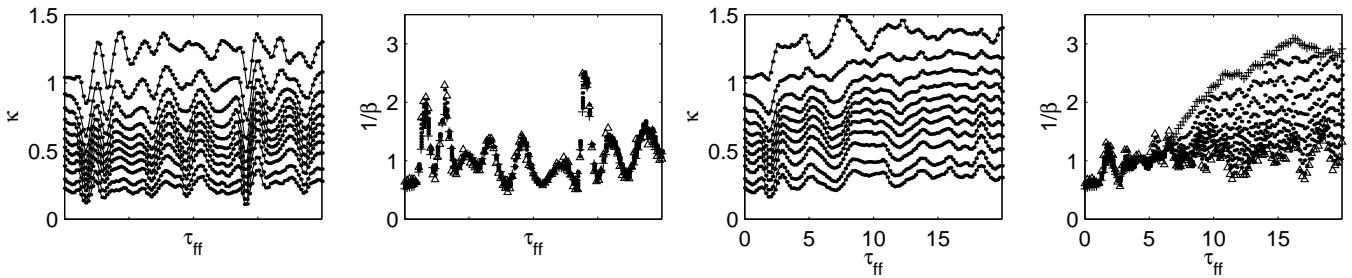


**Fig. 19.** *The two left panels:* Evolution of the Lagrangian radii (left) and the Lagrangian dimensionless temperature (middle left) of a system subjected to an energy-flow and with global dissipation scheme. The curves depict certain mass-fractions, and its temperatures, respectively. The mass fractions, contained in spheres, centered at the center of mass, are:  $\Delta M/M = \{5\%, 10\%, 20\%, \dots, 80\%, 90\%, 98\%\}$ . The triangles (left panel) indicate the temperature of a mass fraction of 5% and the crosses corresponds to a mass fraction of 98%. The simulation is carried out with  $N = 10000$  and  $\epsilon = 0.0046$ . Consequently,  $V_{ff} = 0.001$ , meaning that the system is highly granular. The dynamical range is, 2.3 dex. *The two right panels:* Same as above for a system subjected to an energy-flow and with a local dissipation scheme.

ates The inverse behavior of fragmentation strength and phase-space correlation strength is found in all simulations and is typical for self-gravitating systems.

Finally, systems subject to a permanent energy-flow were studied. We find:

- Typically driven dissipative systems evolve to a high-energy homogeneous phase or undergo a mono-collapse. Yet, model systems with a local energy dissipation can develop persistent phase-space correlations, but a persistent, hierarchical fragmented structure is not observed. This suggests, that matter that has passed through a collapsing transition has to be replenished at large scales in order to maintain a hierarchical structure at molecular cloud scales.

*Acknowledgements.* This work has been supported by the Swiss National Science Foundation.

## References

- Antonov V.A., 1962, Vest. Leningrad Univ. 7, 135; Translation, 1995, IAU Symposium 113, 525
- Aronson E.B., Hansen C.J., 1972, ApJ 177, 145
- Barnes J., Hut P., 1986, Nature 324, 446
- Barnes J., Hut P., 1989, ApJS 70, 389
- Binney J., Tremaine S., 1994, Galactic Dynamics, Princeton University Press, Princeton, New Jersey
- Blitz L., Shu F.H., 1980, ApJ 238, 148
- Blitz L., Williams J.P., 1999, in The Origin of Stars and Planetary Systems, eds. Lada C.J., Kylafis N.D., NATO ASIC Proc. 540, 3, p. 3
- Boghosian B.M., 1999, Braz. J. Phys. 29, 91
- Bolatto A.D., Simon J.D., Leroy A., Blitz L., 2002, ApJ 565, 238
- Bullock J.S., Kravtsov A.V., Weinberg D.H., 2001, ApJ 548, 33
- Chandrasekhar S., 1943, AJ 97, 255
- Chappell D., Scalzo J., 2001, ApJ 551, 712
- Combes F., 1999, CeMDA 72, 91
- Elmegreen B.G., ApJ 530, 277
- de Vega H., Sanchez N., Combes F., 1996, Nature 383, 53
- Dyson J.E., Williams D.A., 1997, The Physics of the Interstellar Medium, Institute of Physics Publishing, Bristol and Philadelphia
- Falgarone E., Perault M., 1987, in Physical Processes in Interstellar Clouds, eds. Morfill T.G.E., Scholer M., Dordrecht: Reidel, 59
- Follana E., Laliena V., 2000, Phys. Rev. E, Vol. 61, 6270
- Fliegans, O., Gross, D.H.E. 2001, cond-mat/0102062
- Fuller G.A., Myers G.A., 1992, ApJ 384, 523
- Glandsdorff P., Prigogine I., 1971, Thermodynamic Theory of Structure, Stability and Fluctuations, Wiley, New York-London

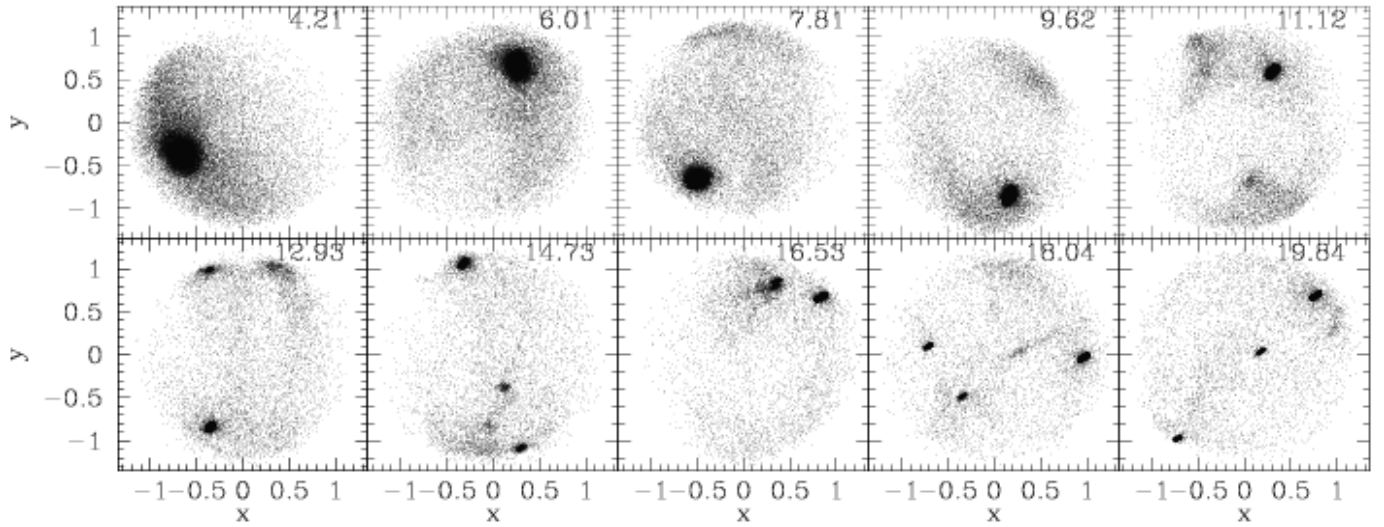


**Fig. 20.** Mass distribution of a system subjected to an energy-flow. Shown is the projection of the particle positions onto the  $xy$ -plane. The particle number is,  $N = 32000$ , and the volume filling factor is,  $V_{ff} = 1$ . Energy is dissipated with a local dissipation scheme,  $\beta = 150$ , and short distance repulsive forces are at work,  $\xi = 2/3$ . The evolution of the corresponding phase-space correlations is shown in Fig. 21. The time is indicated in each panel in units of the free fall time,  $\tau_{ff}$ .

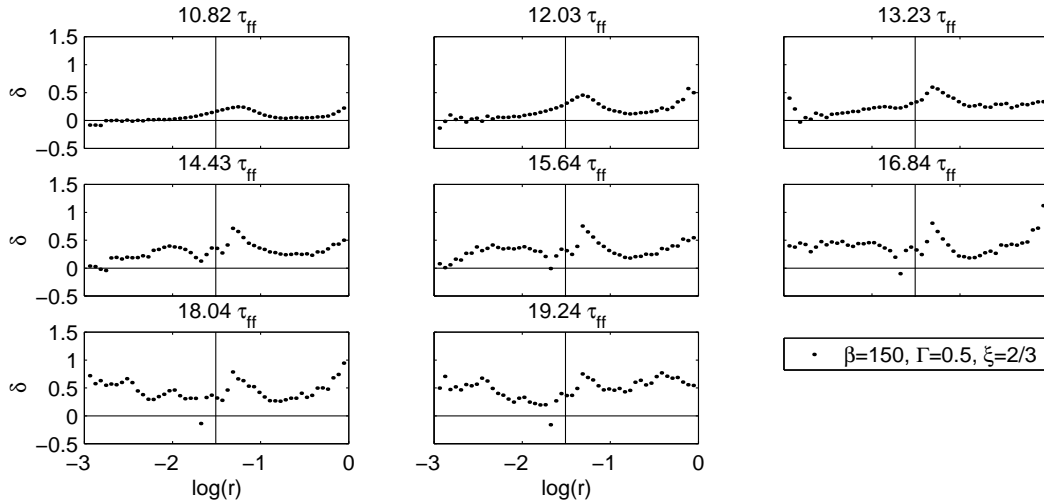


**Fig. 21.** The evolution of the phase-space correlations in a system subjected to an energy-flow and with short distance repulsive forces (see Fig. 20). During the first  $\sim 8 \tau_{ff}$  the index of the velocity-dispersion-size relation is,  $\delta = 0$ , over the whole studied range, then correlations start to grow at largest scales. Finally, the index of the velocity-dispersion-size relation is,  $\delta > 0$ , over the whole dynamical range. In systems subjected to energy-flows, such correlations that extend over the whole dynamical range appear only if a local dissipation scheme is applied.

Hamana T., Yoshida N., Suto Y., 2001, ApJ submitted, astro-ph/0111158  
Hertel P., Thirring W., 1971, in Quanten und Felder, ed. Dürr H.P., Brusanschweig; Hertel P., Thirring W., 1971, CERN preprint TH 1338, 309;  
Huber D., 2001, in The Promise of FIRST, ed. G.L. Pilbratt, J. Cericharo, A.M. Heras, T. Prusti, R.A. Harris, SP-460, ESA Publication Division, The Netherlands, p. 435  
Huber D., Pfenniger D., 2001, in The Promise of FIRST, ed. G.L. Pilbratt, J. Cericharo, A.M. Heras, T. Prusti, R.A. Harris, SP-460, ESA Publication Division, The Netherlands, p. 439  
Huber D., Pfenniger D., 2001, A & A, 374, 465

Klessen R.S., Heitsch F., Mac Low M., 2000, ApJ 535, 887  
Lalena, V. 1999, Phys. Rev. E 59, 4786  
Landsberg, P.T., 1972, Nature 238, 229  
Landsberg, P.T., 1984, J. Stat. Phys. 35, 159  
Larson R.B., 1981, MNRAS 194, 809  
Larson R.B., 2001, in Modes of Star Formation and the Origin of Field Populations, eds. Gerbel E.K., Brandner W., ASP Conf. Ser., astro-ph/0101046  
Latora V., Rapisarda A., Tsallis C., 2001, Phys. Rev. E, Vol. 64, 6134  
Leubner M.P., 2001, astro-ph/0111444  
Lynden-Bell D., Wood R., 1968, MNRAS 138, 495  
Lynden-Bell D., Lynden-Bell R.M., 1977, MNRAS 181, 405

- Lynden-Bell D., 1998, in Proceedings of XXth IUPAP International Conference on Statistical Physics, in print, cond-mat/9812171
- Mandelbrot B., 1982, The Fractal Geometry of Nature, Freeman, San Francisco
- Melo F., Umbanhowar P., Swinney H., 1994, Phys. Rev. Lett. 72, 172
- Miller R.H., 1994, in Ergodic Concepts in Stellar Dynamics, p. 137, eds. Gurzadyan V.G., Pfenniger D., Springer
- Moore B., Ghigna S., Governato F., Lake G., Quinn T., Stadel J., Tozzi P., 1999, ApJ 424, L19
- Myers P.C., Goldman A.A., 1988, ApJ, 329, 392
- Nicolis G., Prigogine I., 1977, Self-Organization in Non-Equilibrium Systems, Wiley, New York
- Padmanabhan T., 1990, Phys. Rep., 188, 285
- Pfenniger D., Combes F., 1994, A&A 285, 94
- Pfenniger D., 1996, in New Extragalactic Perspectives in the New South Africa, eds. Block D.L., Greenberg J.M., Kluwer Academic Publishers, 439
- Pfenniger D., 1998, in: H<sub>2</sub> in the Early Universe, eds. Palla F., Corbelli E., Galli D., Memorie Della Societa Astronomica Italiana, 429
- Plastino A.R., Plastino A., 1999, Braz. J. Phys. 29, 79
- Plummer H.C., 1911, MNRAS, 71, 460
- Prigogine I., 1980, From Being to Becoming: Time and Complexity in the Physical Science, W. H. Freeman & Co., San Francisco
- Safronov V.S., 1960, Ann. d'Astrophysique 23, 979
- Salo H., 1995, Icarus 117, 287
- Scalo J.M., 1985, in Protostars and Planets II, p.201, eds. Black D.C. and Matthews M.S., Univ. of Arizona Press
- Semelin B., Combes F., 2000 A&A 360, 1096
- Sumiyoshi A., Martinez S., Pennini F., Plastino A., Phys. Let. A 281, 126
- Taruya A., Sakagami M., 2001, submitted to Physica A, cond-mat/0107494
- Toomre A., 1964, ApJ 139, 1217
- Toomre A., Kalnajs A.J., 1991, in: Dynamics of Disc Galaxies, p. 341, ed. Sundelius B., Göteborg Univ. Press
- Tsallis C., J. Stat. Phys. 52, 479
- Tsallis C., 1999, Braz. J. Phys. 29, 1
- Vázquez-Semadeni E., 2002, in Seeing Through the Dust: The Detection of HI and the Exploration of the ISM in Galaxies, eds. Taylor R., Landecker T., Willis A., ASP: San Francisco, astro-ph/0201072
- Wisdom J., Tremaine S., 1988, Astron. J. 95, 925